Overview and classification of wavefield seismic imaging methods

PAUL SAVA and STEPHEN J. HILL, Colorado School of Mines

The literature and seismic processing practice overflow with a diversity of wave-equation migration methods. So what makes wave-equation migration a wave-equation migration? What is the commonality of these methods and how do they differ? This article provides a framework for understanding different wave-equation migration methods.

The industry classifies migration algorithms based on the assumptions behind the algorithms, the domain of implementation of the algorithms, and the imaging principle used to create the migrated image. Figure 1 summarizes industry's classification. We turn now to those classifications.

Industry's seismic imaging methods share one fundamental assumption: single scattering at points of discontinuity of impedance in the subsurface. (Impedance equals density times the interval velocity.) We review only single-scattering algorithms, hence assuming multiple-free data.

The customary, conceptual framework of imaging under the single-scattering (or Born) approximation is a "good enough" description of how waves propagate in the subsurface. Despite its intrinsic inaccuracies, this powerful imaging approximation underlies decades of imaging practice.

All migration methods solve an approximate wave equation, the equation that governs the propagation of waves through the Earth. Knowing the velocity of the wave in the Earth and the pressure change as a function of time as recorded by the seismic traces, we may use the wave equation to calculate the pressure change with respect to space.

In general, migration algorithms use the acoustic, and not elastic, wave equation. Because the acoustic wave equation ignores shear waves, its implementation is more straightforward.

This article reviews depth-imaging methods that use either time-domain or frequency-domain numeric solutions to the acoustic wave equation. Our industry terms these "wave-equation migration" methods, distinguishing them from "Kirchhoff migration" techniques that are based on integral numeric solutions to the same acoustic wave equation. Both wave-equation and Kirchhoff migration algorithms solve approximations to the same wave equation.

Kirchhoff migration often uses a ray-tracing shortcut as a quick, approximate wave-equation solution. We cannot remark on the inherent superiority of Kirchhoff versus wave-equation migration because of the wide variety of approximations with both implementations.

Imaging and wavefield reconstruction

In Figure 1, the acoustic wave-equation migration branches into independent or simultaneous wavefield reconstruction. While these two methods use two different imaging conditions, they both depend upon an understanding of the wavefield. In the following paragraphs, we describe separately wavefield reconstruction and the specific imaging conditions for shot-record (independent) and survey-sinking (simultaneous) migrations.

Figure 2 shows a wavefield's position for a single impulse source in a constant-velocity 2D world, as a function of the x coordinate (lateral), the z coordinate (depth), and time t. The red dot (z = 0.0) denotes the location of the source. The

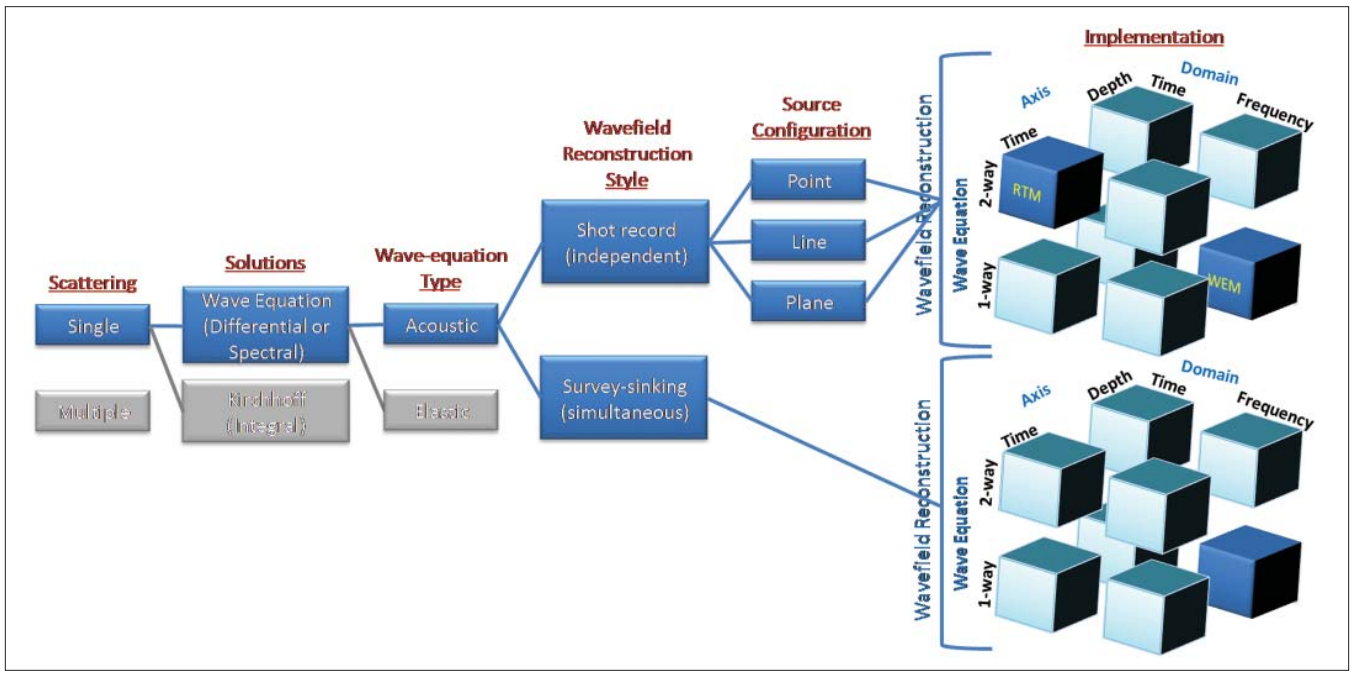

Figure 1. *Classification of migration methods. This paper discusses the migration methods shown in dark blue.*

surface recording is the t-x plane at z = 0.0. The constant depth slices (A and B) in Figure 3 also record diffraction-like shapes. The time slices (A and B) in Figure 4 are two frames from a movie recording the spherical wavefront's propagation.

Shot-record migration

Wave-equation migration algorithms create a subsurface image from full, multidimensional wavefields and an imaging condition. Two different imaging conditions give rise to two different migration procedures. Figure 6 explains the operation of the first procedure, shot-record (sequential imaging) migration. The following refers to the lettered blue dots in Figure 6.

a) Assume a constant-velocity world, containing a horizontal, and a deeper, dipping reflector observed on a 2D, split-spread shot record. The receivers are in the x direction. While the following reasoning also applies to 3D shot records, 2D eases the visualization task.

b) Following the firing of an impulsive surface source (t = 0), surface receivers record two reflections, one from each reflector.

c) The single, red dot (t = 0) represents the source impulse on its t, x "data" recording. This source specification, an impulse in this case, is "data" just as the receiver record are data.

d) With the surface recording as a boundary condition and knowledge of the velocity, the wave equation generates the wavefield, W_R, as a function of x, z, and t. This figure color-codes the individual wavefields with the respective "colors" of the two reflectors. For this constant-velocity world, the wavefields are cones, radiating from the t = 0 positions of each reflector's image of the single surface source.

e) From knowledge of the surface impulsive source, the wave equation generates the source wavefield, W_S. For this constant-velocity world, the wavefield is a cone, radiating from t = 0 and the source's lateral location.

f) and **g)** The imaging condition for this algorithm states that a scattering point exists at the spatial coordinate (x and z) that contains coincident, nonzero wavefield amplitudes in both the source and the receiver wavefields. Thinking in terms of a single reflector (Figure 5), the wavefield originating from the source (S) is incident upon the reflector at the same location and instant that the reflected, receiver (R) wavefield reflects from that reflector. At a reflection point (x, z), the source and the receiver wavefields are both nonzero at the same time, t. The particular value of the time, t, is immaterial to the existence of the reflection point at x, y, only that the wavefields coincided at some time, t. To determine a time-coincident amplitude in both the source and receiver wavefields, the algorithm crosscorrelates the two wavefields as a function of time for all x, z locations. Figure 6f and Figure 6g show the intersection of x and z planes, defining a specific x = x*, z = z* crosscorrelation coordinate. The receiver wavefield $W_R(x^*, x^*)$ contains two nonzero amplitudes (Figure 6f), corresponding to the pair of reflectors. The source wavefield $W_S(x^*, x^*)$ contains a single, nonzero amplitude (Figure 6g). For this x*, z* location on the shallower reflector, the time coincidence of the nonzero amplitudes of the source and receiver wavefields creates the crosscorrelation's nonzero value.

h) This figure posts the nonzero value of the crosscorrelation coefficient at the x*, z* location, the depth of the shallower, horizontal reflector. Sequentially crosscorrelating the source and the receiver wavefields amplitudes as a function of time over possible x and z locations images the x, z plane in Figure 6h. For this 2D example, these successive crosscorrelations create a subsurface image from a seismic experiment (shot record). For 3D data, the above workflow generalizes, using 4D wavefields.

Figure 6 does not illustrate the final step, the summation of each of the images (Figure 6h) created from each seismic experiment (shot record.) If a 3D survey contains 1000 shot records, then duplicate the workflow in Figure 6 a thousand times.

The literature sometimes refers to this imaging model as the "WRW" model (Berkhout, 1982), which in our nomen-

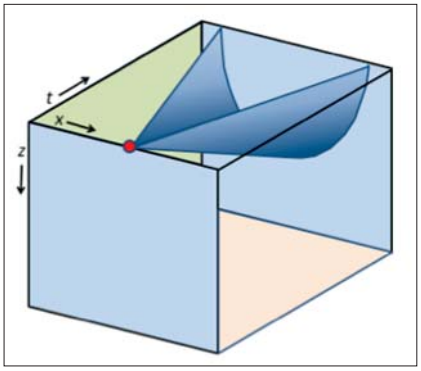

Figure 2. *Wavefield of a single impulse source.*

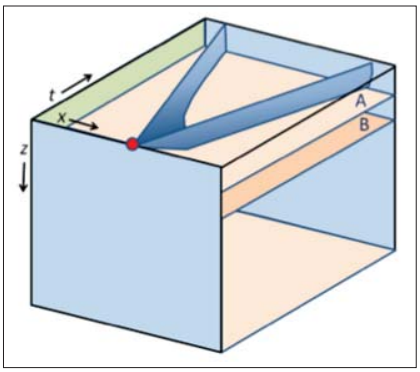

Figure 3. *Two depth slices through a wavefield of a single impulse source.*

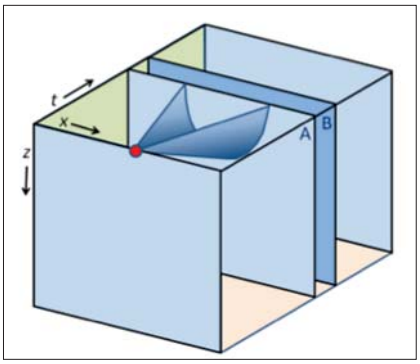

Figure 4. *Two time slices of a wavefield of a single impulse source.*

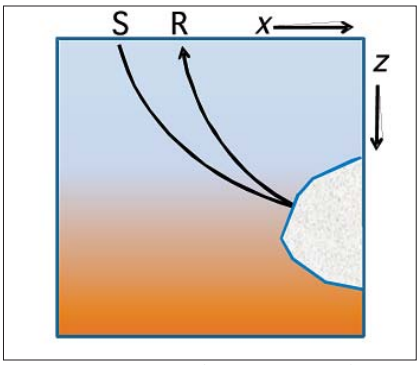

Figure 5. *Source and receiver raypaths.*

clature would be termed the W_S-R-W_R model, with the inner "R" referring to the desired reflectivity. The key elements for seismic migration are the source and scattered wavefields, because they are, respectively, the generator and carrier of information from the subsurface to the recording surface. For 3D data, both wavefields are four-dimensional functions of position in space (x, y, z) and time (t).

Generalizing, Figure 6 provides the two components of a generic, independent wave-equation migration procedure:

1) Wavefield reconstruction that generates the source and scattered wavefields, W_S and W_R, at all locations in space x, y, z, and all times t from data recorded at the surface
2) An imaging condition that extracts reflectivity information (i.e, the image I) from the reconstructed source and scattered wavefields W_S and W_R.

The next sections provide more information about the imaging principle and the wavefield reconstruction step for this shot-record migration method.

Imaging principle

The two wavefield volumes provide the imaging input. Through the single-scattering assumption, the wavefields share an important characteristic: within an amplitude scale factor that depends on the value of the reflection coefficient, the two wavefields are equivalent at the reflectors. This is the imaging principle. In describing this imaging principle, migration experts state that the two wavefields are kinematically equivalent at the reflector positions. In this context, kinematically means that the timings, but not the amplitudes, are identical.

Identifying amplitudes coincident in time at a specified position in space is the underlying principle for conventional imaging. The moment of wavefield time coincidence depends on the position of the reflectors and on the velocity characterizing wave propagation in the subsurface, which are unknown a priori.

Conceptually, in the search for reflectors we assume that we can compute and analyze the source and scattered (receiver) wavefields at every location in space (x, y, z), and time (t). In implementation, the algorithms never store the entirety of two wavefields in the computer, but store wavefield subsets at select locations, times (or frequencies) and compute and analyze them sequentially.

Wavefield reconstruction

Using a velocity model of the subsurface, wavefield reconstruction simulates wave propagation, as a function of space and time, using a wave-equation that is appropriate for the type of wave under consideration. For example, acoustic wavefield reconstruction requires the acoustic wave equation while elastic wavefield reconstruction uses the elastic wave equation, each with appropriate subsurface velocities.

The migration algorithm creates the source wavefield (left side of Figure 6) by modeling seismic waves propagating forward in time, assuming a known source location, source wavelet, and a subsurface velocity model. In simulating the source wavefield forward in time, the migration algorithm simulates the firing of the source and records the propagation of the wavefield as time increases. Implementation differences in wavefield reconstruction algorithms simulate the source wavefields forward in time.

The migration algorithm reconstructs the scattered wavefield (right side of Figure 6) by modeling the recorded seismic waves backward in time, with known receiver locations, the recorded data, and an assumed subsurface velocity model. In simulating the receiver wavefield backward in time, the migration algorithm converts the surface receivers into sources. If you will, imagine a movie of the reflected wavefront approaching and then recorded by the surface receivers. Now, run that movie backwards in time. This time-reversed movie shows the surface generating a wavefield that propagates towards the reflectors. The migration algorithm simulates that time-reversed movie by converting the true receivers into sources, and, using the surface recordings, generates the time-reverse of the wavefield.

The migration algorithm uses the output of wavefield reconstruction as input for the imaging condition procedure. Having generated the source and receiver wavefields, the migration algorithm identifies the positions of temporal coincidence of the amplitudes at subsurface locations.

Successful wavefield reconstruction relies on the single-scattering assumption for seismic imaging, i.e.:

- Recorded wavefields have scattered only once in the subsurface (there are no multiples in the data).
- No scattering occurs in the process of wavefield reconstruction.

Violating either assumption creates extraneous reflections. Thus, multiple attenuation before migration is critical.

The right side of Figure 1 shows three ways to classify wavefield reconstruction techniques.

Wave-equation approximation

An algorithm may use the more accurate two-way wave equation or the simpler, and computationally faster, one-way wave equation. The two-way wave equation solves for waves traveling in all directions while the one-way wave equation solves for waves propagating mainly in the vertical direction.

As implemented, both the one-way and the two-way wave equations approximate the wave equation. Both equations contain approximations of the medium in addition to the prevalent direction of wave propagation in order to convert the wave equation's differential equation into a digital form for execution on a digital computer.

Reconstruction axis

We also classify wavefield reconstruction methods according to the order of calculation. In all cases, the algorithms create a 4D wavefield from 3D data. The time-marching wavefield extrapolation method progressively reconstructs the wavefield in time for all x, y, z. The depth-marching wavefield ex-

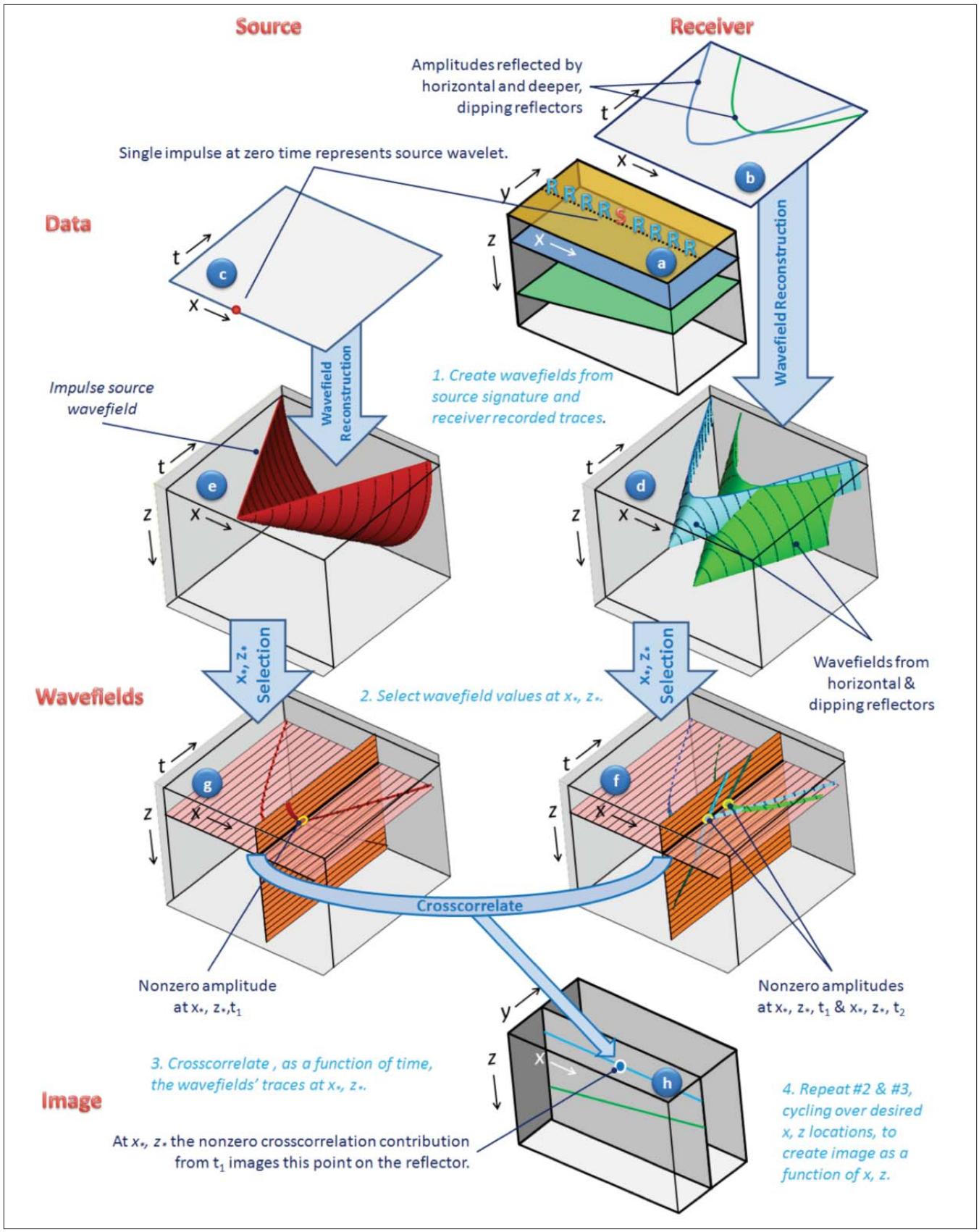

Figure 6. *Shot-record, wave-equation migration through sequential imaging.*

trapolation method progressively reconstructs the wavefield in depth for all x, y, t.

To understand the differences in these two approaches, contrast Figure 3 with Figure 4. Figure 3 reconstructs the impulse-source wavefield of Figure 2 through a depth-marching scheme. In this figure, the algorithm has reconstructed the wavefield from the surface, z = 0 to a depth z = z_A as a function of time and lateral position, x. Slice A's wavefield is a diffraction. The algorithm's wave equation estimates the wavefield at the next increment of depth, on depth slice B.

Figure 4 reconstructs the impulse-source wavefield with a time-marching scheme. Assume the algorithm reconstructed the wavefield from t = 0.0 to t_A, where time t = t_A is the constant-time slice labeled A. For this simple, constant-velocity case, the reconstructed wavefield at time t = t_A is a hemisphere. Knowing the wavefield at time slice A for all values of x and z, the algorithm's wave equation estimates the wavefield at the next increment of time, at t = t_B, on time slice B.

Reconstruction domain

A third way of classifying wavefield reconstruction methods specifies the domain of wavefield reconstruction. There are time-space (*t-x*) methods, frequency-space (*f-x*) methods, frequency-wavenumber (*f-k*) methods, or mixed frequency-wavenumber/frequency-space (*f-k/f-x*) methods. A method's applicability depends on the velocity model's assumptions. For example, the time-space methods honor the velocity model at each x, y, z location. While the frequency-domain methods may decrease the computer execution times, they approximate the velocity model as a series of constant-velocity layers. Mixed-domain methods relax this assumption.

As an aside, note that the source and scattered wavefields need not be reconstructed with identical techniques. An algorithm could, for example, use a t-x method to simulate the source wavefield and an f-x method to reconstruct the scattered wavefield, without change to the generic imaging scheme shown in Figure 6.

Because they often occur together, two combinations of the wavefield-reconstruction methods shown in the right of Figure 1 have their own shorthand names.

- Reverse-time migration is characterized by time-marching wavefield reconstruction using a two-way (acoustic) wave equation, with numeric solutions implemented in the time domain.
- Migration by wavefield extrapolation is characterized by depth-marching wavefield reconstruction, using a one-way wave equation, with solutions implemented in the frequency domain.

Extended imaging conditions

As used above, the conventional imaging condition computes the zero lag of the local crosscorrelation between the source and scattered wavefields at the same x, y, z locations. That crosscorrelation converts the individual wavefields in Figures 6f and 6g into the image in Figure 6h. The "zero lag" means that no spatial or time shift exists between the two wavefields before the cross-correlation. In mathematical form, the conventional imaging condition uses wavefield crosscorrelation to create an image, I:

$$I(x,y,z) = \int W_S(x,y,z,t) \cdot W_R(x,y,z,t)dt. \quad (1)$$

The industry extensively uses this conventional imaging condition. It is usually referred to as imaging at "zero time and zero offset" (Claerbout, 1985), where in this situation, the word "offset" is the physical separation (lag) between the source and scattered wavefields.

Other imaging conditions may differ from the conventional imaging condition in two regards. The first is in the mathematics of determining similarity and the second is in exploring nonzero lags in the crosscorrelation. Considering the implementation deviation, other mathematical tools such as deconvolution, may numerically estimate the similarity of the two wavefields.

The second departure from the conventional imaging condition extends the imaging condition into a more general imaging condition, sometimes referred to as an extended imaging condition. The extended imaging condition uses nonzero lags in the crosscorrelation. In mathematical form, it is,

$$I(x, y, z, \lambda_x, \lambda_y, \lambda_z, \tau) = \int W_S(x-\lambda_x, y-\lambda_y, z-\lambda_z, t-\tau) \cdot W_R(x+\lambda_x, y+\lambda_y, z+\lambda_z, t+\tau)dt, \quad (2)$$

where the formed image I depends not only on the physical coordinates x, y, z, but also the space lags (λ_x, λ_y, λ_z) and the time lag τ. Referring to Figure 6, Equation 2 shifts the source and receiver wavefields with respect to each other in the space and time coordinates before the pairwise crosscorrelation. The extended imaging condition embodies the conventional imaging condition as a subset, for the case of zero lags in space and time.

This extended imaging condition has two uses. First, practitioners use the multidimensional image, I(*x, y, z, x, y, z,* λ_x, λ_y, λ_z) as an ingredient in amplitude-versus-angle determination, which we discuss in a later paragraph. Second, practitioners determine wavefield reconstruction error. Wavefield reconstruction errors may exist

- if we use inaccurate wavefield reconstruction methods (e.g., methods based on low-order, one-way, wave-equation wavefield extrapolators)
- if we use inaccurate velocity models for wavefield reconstruction
- if we violate the single-scattering model (i.e., multiples exist in the data or if they are being generated in the process of wavefield reconstruction)
- if we inadequately sample the scattered (reflected) wavefield on the acquisition surface (i.e., truncating acquisition at cable ends or avoiding obstacles on the acquisition surface)
- if not all the scattered wavefield propagates to the acquisition surface (incomplete subsurface illumination)

Assuming no errors in the wavefield reconstruction, the

wavefield crosscorrelation maximizes at zero lag (in space and time). For the error-free case, Equation 2, I is a maximum when $\lambda_x, \lambda_y, \lambda_z$ and time lag τ all equal zero. Otherwise, wavefield reconstruction errors will cause the local crosscorrelation to spread at nonzero lags, indicating one or more errors in wavefield reconstruction. Typically, simultaneous, multiple wavefield reconstruction errors make it difficult to use the extended imaging condition to diagnose their origin.

In the absence of wavefield reconstruction errors, practitioners estimate amplitude variation with angle from the extended imaging condition. The algorithm constructs angle-domain, common-image gathers, representing the angle-dependent reflectivity at every point in the subsurface. Therefore, practitioners can use these angle-domain common-image gathers for AVA analysis in media of arbitrary complexity or as the basis for model updating using migration velocity analysis. By contrast, the application of the conventional imaging condition corresponds to a stack over all scattering angles of the image.

The selection of a particular imaging condition implementation (conventional or extended, crosscorrelation or deconvolution) is independent of the selection of the wavefield reconstruction methods. For example, any imaging conditions described in this section can be applied equally well to reverse-time imaging methods or to downward-continuation imaging methods summarized in Figure 1.

Seismic experiment examples

The imaging procedure depicted in Figure 6 illustrates the implementation for a specific shot record, a natural seismic experiment. For shot-record-based acquisition, the superposition of shot-record-based images creates a final, migrated image.

The generic imaging procedure shown in Figure 6 is not restricted to the single-source geometry. Practitioners use the same generic imaging scheme for other source configurations, for example a line or a plane source. The following summarizes the possible source configurations and their associated migration terminologies:

- Point source: The algorithm separately images the data acquired for individual shots. The literature terms this "shot-record migration." Figure 6 illustrated this implementation.
- Line source: The algorithm combines data acquired for shots located along a single direction with appropriate 1D space-time delays into simulated recorded data. The literature terms this "delay-line migration."
- Plane source: The algorithm combines data acquired for shots distributed over a specified spatial patch with appropriate 2D space-time delays to create simulated recorded data. The literature terms this "plane-wave migration."

Other types of synthesized sources and associated migrations are possible, e.g., based on data from different shots combined with random space-time delays. These synthetic source combinations may reduce the required computer resources by more efficiently using the recorded shots and exploiting the redundancy characterizing acquired data.

For all synthesized source procedures, the imaging procedure follows the same pattern (Figure 6), starting with wavefield reconstruction of source and scattered wavefields, followed by an imaging condition application. Instead of creating a source wavefield for an isolated, point source, such as idealized in Figure 6, the simulated array of sources drives the source wavefield reconstruction. For example, migration algorithms may implement plane-wave migration through depth-marching, one-way extrapolation in the frequency domain, thus described as wavefield-extrapolation migration (WEM in Figure 1). Alternatively, migration algorithms may implement plane-wave migration through time-marching, two-way extrapolation in the time domain, thus described as reverse-time migration (RTM in Figure 1).

Simulating different sources adds an additional dimension to the specification of a particular migration algorithm. To review, we specify a wave-equation migration algorithm by its wavefield reconstruction axis, its wavefield reconstruction domain, its wavefield reconstruction equation, its imaging condition, and its source configuration. With these five different "specification domains" for a migration implementation, no wonder GEOPHYSICS contains an abundance of migration papers. Moreover, this is not an exhaustive list of "specifications domains."

Shot-record computational cost

Imaging accuracy and computational cost are the main considerations for selecting a specific wavefield-reconstruction/imaging-condition combination. Typically, the trade-off is between higher accuracy and higher computational cost. One often follows the other. The following compares the computational cost of various wave-equation imaging methods. This comparison does not include the important practical considerations of data storage, speed of data transfer, computing parallelization models, etc.

The cost of shot-record migration (C_{SRM}) is

$$C_{SRM} \sim N_e\,(2C_{WR} + C_{IC}) \qquad (3)$$

where N_e is the number of experiments (e.g., shots or lines or planes) to construct a complete image; C_{WR} is the computational cost of source or receiver wavefield reconstruction; and C_{IC} is the computational cost of the imaging condition. This equation makes the simplifying assumption that each individual shot illuminates the entire seismic volume, and hence the shot-record algorithm creates an image of the entire seismic volume from each shot record. In practice, a given shot illuminates only a portion of the total, desired volume, and thus it is not necessary to create an image of the entire seismic survey volume from each, individual shot record.

Typically, the number of acquired shots is larger than the number of simulated plane sources; therefore, a plane-wave implementation usually provides a more efficient imaging procedure by reducing N_e. Because the wavefield reconstruc-

tion cost is typically significantly higher than the imaging condition cost, the following analyzes C_{WR}.

Wavefield reconstruction's cost is proportional to the reconstructed wavefield's size. For example, if the algorithm reconstructs the wavefields with a time-marching method, the wavefield reconstruction cost is

$$C_{WR} \sim (N_x N_y N_z) N_t \quad (4)$$

where N_x, N_y, N_z represent the dimensions of the reconstructed wavefields along the space axes, and N_t represents the dimension of the reconstructed wavefields along the time axis. The wavefield reconstruction cost for a frequency-domain depth-marching method is

$$C_{WR} \sim (N_x N_y N_z) N_f \quad (5)$$

where N_f represents the dimension of the reconstructed cube along the frequency axis. Typically, N_f is smaller than N_t; therefore, the cost of frequency-domain wavefield reconstruction is smaller than the cost of time-domain wavefield reconstruction.

Combining Equation 3 and Equation 5, under the assumption that the application of the imaging condition is "free," we have

$$C_{SRM} \sim N_e (N_x N_y N_z) N_f \quad (6)$$

The preceding discussion assumes that the lateral extent of the reconstructed wavefields is the same for all reconstruction methods. In practice, this is not true. For example, plane-wave migration often covers a larger aperture than shot-record migration. Therefore, the computational gain achieved by plane-wave migration relative to shot-record migration due to the smaller number of experiments is reduced due to the larger aperture involved in imaging. Thus, to achieve high computational gains, image seismic data using the following prescription:

1) plane-wave method (with as small a number of plane waves as possible)
2) one-way wavefield extrapolation in the frequency domain (with as small a number of frequencies as possible)
3) a limited aperture (as small as possible to allow for wave propagation needed to image the steepest reflectors in the required target)

However, if the accuracy of the frequency-domain implementation is insufficient to image the target, then employ implementations that are more accurate, at associated higher computational cost.

Shot-record example

Figure 7 shows wave-equation imaging of the Marmousi model as implemented with reverse-time migration. Figure 7 follows the organization in Figure 6.

Figure 7a is the Marmousi model with the lighter grey representing regions of larger impedance. Ray-tracing rays overlay the model to demonstrate uneven illumination.

Figure 7b is the modeled data, recorded from a uniform distribution of surface receivers. Those data depend on the source type, the velocity model, and the subsurface distribution of reflectors.

As discussed in the preceding section, shot-record migration accommodates a localized or a distributed source. Figure 7c is a localized, point source.

Figure 7d represents the scattered (receiver) wavefield reconstructed through reverse-time propagation of the recorded data in Figure 7b. The organization of this 3D plot deserves explanation. The data projected on the surface of this 3D figure actually are the data residing within the volume. The two dotted lines on each 2D slice denote the positions of the extractions of the represented data.

Figure 7e is the source wavefield estimated by propagating the source data (Figure 7c) forward in time.

Figure 7f represents the migrated image estimated from the zero-lag, temporal, crosscorrelation of the source and scattered wavefields (Figure 7d and Figure 7e).

Simultaneous imaging of seismic experiments

We now turn to a different imaging method, with its own imaging condition. The previously presented method uses a succession of single seismic experiments, creating successive images that are then composited into a final image. The "seismic experiment" may be a shot record or a plane-wave record, for example. In all cases, the method assumes that data provide consistent and redundant coverage of the subsurface and that summation of the individual experiment's images produce a final image.

By contrast, an alternative approach creates an image from the simultaneous use of all of the data. This second approach may be termed "survey sinking" because it uses the wave equation to create new "observed" data, as if the acquisition were deeper in the Earth.

Figure 8 illustrates this survey sinking method.

a) As was the case with Figure 6, this figure also represents a pair of subsurface reflectors, one horizontal, and one dipping. The distribution of surface sources and receivers represents the acquisition of a collection of 3D shot records. The survey-sinking algorithm simultaneously operates on all shot records.
b) Following the name, "survey sinking," the algorithm uses the wave equation to create new data as if the entire survey were acquired at a series of deeper depths in the Earth. This figure shows three different observation planes: first, the initial observation plane; second, an observation plane at an intermediate depth between the surface and the shallower reflector; third, an observation plane on the horizontal (blue) reflector (shown slightly displaced above it for clarity).
c) This figure shows two subvolumes extracted from a 5D volume that contains amplitudes as a function of x_s, y_s, x_r, y_r, and t. The subscripts refer to the source (s) or receiver (r) coordinates. Figure 8c left is the zero-offset subvolume.

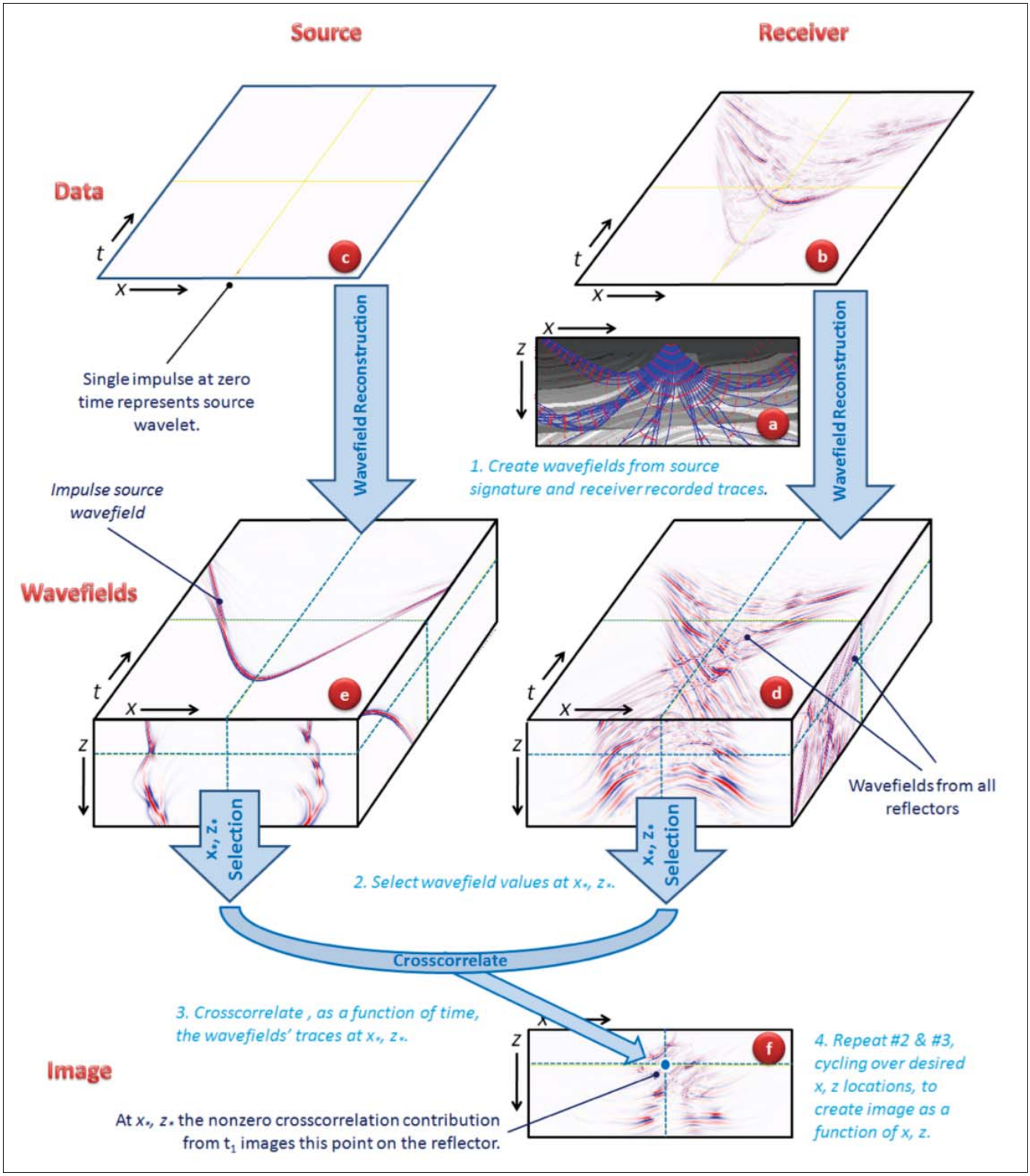

Figure 7. *Shot record migration of Marmousi model.*

This subvolume shows the horizontal and the dipping reflectors as a function of time as observed from zero-offset geometry. Figure 8c is an offset volume for a source-receiver midpoint in the center of Figure 8b. This subvolume displays only positive x y offsets. The horizontal reflector is symmetric about zero offset. Using this blue reflector's moveout as a reference, observe asymmetric moveout for the dipping reflector. The dipping reflector's moveout is less in the dip (y) direction.

d) These subvolumes are from a new 5D volume, representing the observations from Figure 8b's second displayed observation plane. Using data from the original observation

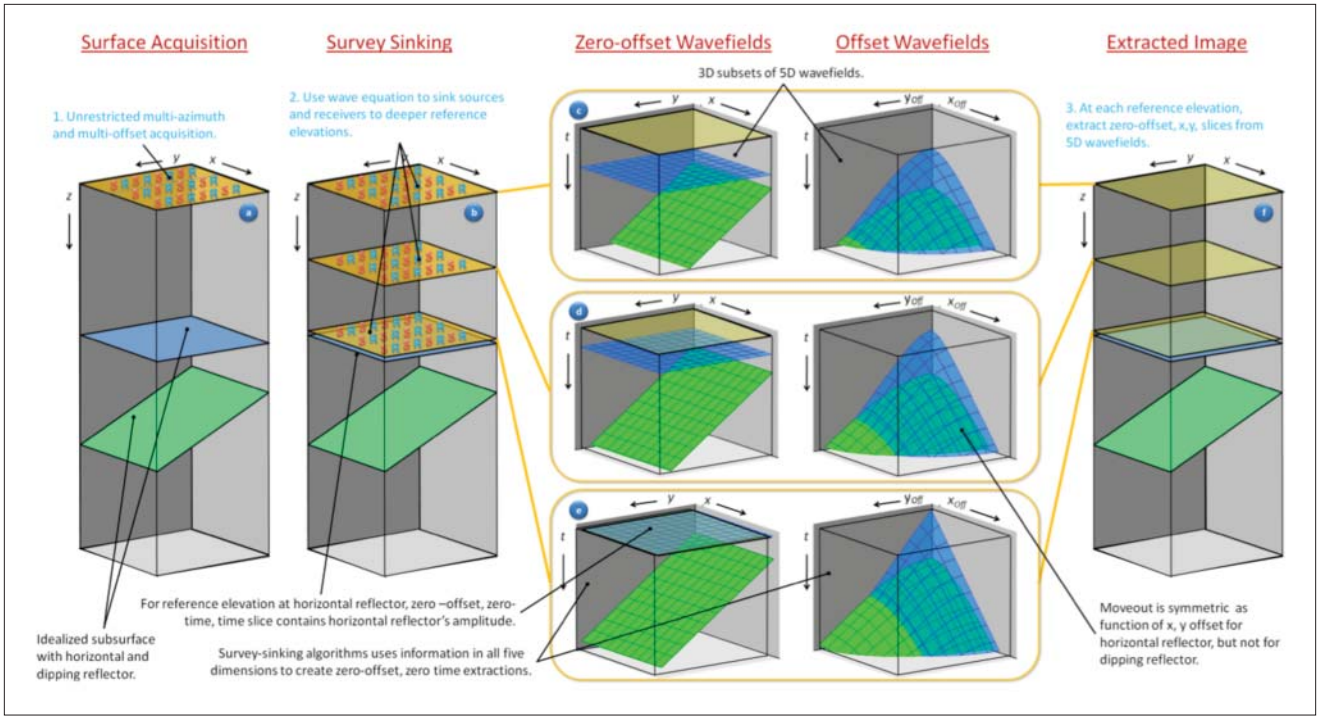

Figure 8. *Survey-sinking migration.*

plane (Figure 8c) and a velocity model, the wave equation creates these "survey-sunk" data. Comparing to Figure 8c, the reflector times decrease as the reference elevation approaches the depths of the two reflectors. In addition, the relative moveout delay as a function of offset increased.

e) These subvolumes contain the observations for Figure 8b's deepest displayed observation plane. The application of the wave equation creates these "survey-sunk" data from the previously calculated data of Figure 8d and the velocity model between the reference elevations in Figures 8d and 8e. As before, as the reference elevation sinks, approaching the two reflectors, the reflectors' timing decreases. With the reference elevation at the depth of the horizontal reflector, the zero-offset observations of that reflector appear at zero time.

If we were to continue to sink the survey below the depth of the (blue) horizontal reflector, then the 5D volume would no longer contain reflected amplitudes from that horizontal reflector, but only the deeper (green) reflector. As the reference depth progresses through the deeper reflector, its zero-offset amplitudes would be visible at zero time and the x, y locations of the intersection of the reference elevation with the reflector. If the reference elevation were entirely beneath the depth of the dipping reflector, then the 5D volume would contain zero amplitude.

f) For this survey-sinking migration, the imaging condition extracts the zero-time, zero-offset amplitudes at the respective "survey-sunk" reference elevations. This imaging condition arises from a simple observation. If we were to acquire a survey immediately on top of a given reflector, that reflector would be visible in the acquired, zero-offset traces at zero time. Employing this imaging condition, the migration algorithm extracts the zero-time, zero-offset amplitude and posts it in the depth volume (Figure 8f) at the respective x, y locations for each "sunk" depth, z. Figure 8f illustrates the extraction of those amplitudes for three different reference depths.

In summary, the survey-sinking method uses the wave equation to create successively deeper observations. Its imaging condition extracts the zero-time, zero-offset amplitudes for the depths of interest.

The successive downward continuations and amplitude extractions of the survey-sinking method consume significant computer time and memory. According to Figure 8, the algorithm recalculates all of the "observed" data at each depth of interest. Therefore, practitioners do not implement the algorithm in the time domain, as implied by Figure 8, but find significant efficiencies in converting the data to the frequency domain. In the frequency domain, they implement the downward continuations through successive phase-shift operations, one frequency at a time. Inverse Fourier transforms to zero time provides the depth image.

In contrast to the shot-record method, survey-sinking simultaneously images the subsurface using the entire collection of seismic experiments (shot records.) The shot-record migration requires a final summation of the individual shot-record images to create the final image. For both algorithms, the overall mechanism of imaging uses the same two steps: wavefield reconstruction at all locations in the subsurface from recorded data, followed by an imaging condition, extracting reflectivity information from the reconstructed wavefields. Assuming single scattering in the subsurface, independent imaging with single seismic experiments and simultaneous

imaging with all seismic experiments produce equivalent images of the subsurface.

Survey-sinking computational cost

Survey-sinking and shot-record migrations use the same data for imaging; however, survey-sinking migration simultaneously images all seismic shots at a time. To determine the relative cost of survey-sinking migration, we recognize wavefield reconstruction dominates imaging cost. Each trace has four independent coordinates, the midpoints x, y and the offsets h_x and h_y. For comparison purposes, we assume that the midpoint grid and the imaging grid are the same, which is consistent with imaging practice. The total cost of wavefield reconstruction in survey-sinking imaging is

$$C_{SSM} \sim (N_{hx}\, N_{hy})\, (N_x\, N_y\, N_z)\, N_f \qquad (7)$$

where $(N_x\, N_y\, N_z)$ is the size of the imaged volume, N_f represents the number of frequencies, and $(N_{hx}\, N_{hy})$ is the number of offsets of the imaged data set.

Survey-sinking versus shot-record migration

Equation 6 and Equation 7 provide the relative cost comparisons between survey-sinking and shot-record migration. The choice depends on several factors, including:

1) Shot sampling. With sparsely sampled shots, then the number of shots, N_e, is small, then shot-record imaging is preferred. Otherwise, for a large number of shots, survey-sinking migration is more computationally efficient.
2) Offset size. If large offsets characterize the acquired data, then the choice between shot-record and survey-sinking migration drives the relative size of the number of shots, N_e, and the number of offsets $(N_{hx}\, N_{hy})$ drives the choice between shot-record and survey-sinking migration. This choice is contingent upon the availability of computers capable of processing the necessary data volume.
3) Computer memory. If the computers available for processing have small memory, then shot-record imaging is the only feasible option. Otherwise, survey-sinking migration might be the preferred solution, depending on offset size and shot-sampling criteria discussed earlier.

Common-azimuth migration

Reducing the size of the reconstructed wavelet will speed up survey-sinking migration. "Common-azimuth" migration assumes data are along a common azimuth, i.e., the lines connecting all shot-receiver pairs align in a fixed direction. Conventional streamer acquisition often comes close to satisfying this assumption. We may rotate data that do not conform to this assumption before migration in order to align along one preferential azimuth. In addition, common-azimuth migration assumes preservation of that common azimuth as we sink the survey using frequency-domain downward continuation. This stronger assumption is also not always fulfilled, especially in areas with large lateral velocity gradients, e.g. in regions with salt geology. Following the preceding section's argument, the cost of common-azimuth imaging is

$$C_{CAM} \sim (N_h)\, (N_x\, N_y\, N_z)\, N_f \qquad (8)$$

where N_h represents the number of offsets. This technique achieves an order-of-magnitude cost reduction for wavefield reconstruction relative to conventional survey-sinking migration, at the expense of simplifying assumptions about wave propagation in the subsurface.

Narrow-azimuth migration

Narrow-azimuth migration is a costlier, but more accurate variation of common-azimuth, survey-sinking migration. Narrow-azimuth migration relaxes the common-azimuth assumption. Narrow-azimuth migration assumes data are along a narrow range of azimuths around a preferential direction and remain confined within the original narrow-azimuth band during survey sinking. While this is a more generous assumption than common-azimuth migration's assumption, there is no guarantee that this practice fulfills this condition, especially in areas with large velocity gradients. Similarly to

the earlier discussion, the cost of narrow-azimuth migration is

$$C_{NAM} \sim (N_h N_a) (N_x N_y N_z) N_f \quad (9)$$

where N_a represents the number of azimuths characterizing the acquired data.

Neither common-azimuth nor narrow-azimuth migration are applicable for data acquired with modern wide-azimuth geometries. In these cases, the practical imaging solutions use independent imaging of seismic experiments, i.e., using single shot sources, line sources, or plane sources.

Summary

Wave-equation imaging techniques based on the single-scattering approximation are more similar to each other than they appear at first glance. All methods follow a common processing scheme comprising of two steps: wavefield reconstruction and imaging condition. Figure 6 illustrates shot-record migration with its independent source and receiver wavefield reconstruction. Figure 8 illustrates survey-sinking algorithms. Wavefields are reconstructed recursively by marching in space or time, based on different types of wave equation solved in the time or frequency domain using numeric solutions of various degrees of accuracy. The cost of wavefield reconstruction is proportional to the size of the wavefield and this usually dominates the cost of imaging.

The two different methods employ two different imaging conditions. For the shot-record migration, the imaging condition extracts reflectivity information by comparing reconstructed source and scattered wavefields at every location in space to identify wavefield components that match kinematically. We may generalize this imaging condition to calculate the crosscorrelations at various lags in space and time, obtaining information for velocity or amplitude analysis.

The survey-sinking imaging condition states that our observation point is coincident with a reflector when we observe that reflector at zero time and zero offset.

Suggested reading. *Imaging the Earth's Interior* by Claerbout (Blackwell, 1985). *Imaging of Acoustic Energy by Wavefield Extrapolation* by Berkhout (Elsevier, 1982). *Seismic Migration: Theory and Practice* by Stolt and Benson (Pergamon, 1986). *Seismic Data Analysis* by Yilmaz (SEG, 2001). *3D Seismic Imaging* by Biondi (SEG, 2006).

We invite readers to visit the online companion of this paper at *www.mines.edu/~psava/*. The Web page contains more details and updates to the material presented here, as well as animated-imaging examples. TLE

Acknowledgments: We constructed all examples using the Madagascar software package, freely available from www.reproducibility.org.

Corresponding author: psava@mines.edu